AIP Journal of Applied Physics

A model for hysteretic magnetic properties under the application of noncoaxial stress and field

M. J. Sablik, S. W. Rubin, L. A. Riley, D. C. Jiles, D. A. Kaminski, and S. B. Biner

Citation: Journal of Applied Physics **74**, 480 (1993); doi: 10.1063/1.355257
View online: http://dx.doi.org/10.1063/1.355257
View Table of Contents: http://scitation.aip.org/content/aip/journal/jap/74/1?ver=pdfcov
Published by the AIP Publishing

A model for hysteretic magnetic properties under the application of noncoaxial stress and field

M. J. Sablik, S. W. Rubin, and L. A. Riley
Southwest Research Institute, P.O. Drawer 28510, San Antonio, Texas 78228-0510

D. C. Jiles, D. A. Kaminski, and S. B. Biner
Center for NDE, Iowa State University, Ames, Iowa 50011

(Received 15 December 1992; accepted for publication 20 March 1993)

Although descriptions of the effect of stress on spontaneous magnetization within a single domain already exist, there remains no adequate mathematical model for the effects of noncoaxial magnetic field and stress on bulk magnetization in a multidomained specimen. This article addresses the problem and provides a phenomenological theory that applies to the case of bulk isotropic materials. The magnetomechanical hysteresis model of Sablik and Jiles is thus extended to treat magnetic properties in the case of noncoaxial stress and magnetic field in an isotropic, polycrystalline medium. In the modeling, noncollinearity between magnetization and magnetic field is taken into account. The effect of roll-axis anisotropy is also considered. Both magnetic and magnetostrictive hysteresis are describable by the extended model. Emphasis in this article is on describing properties like coercivity, remanence, hysteresis loss, maximum flux density, and maximum differential permeability as a function of stress for various angular orientations between field and stress axis. The model predictions are compared with experimental results.

I. INTRODUCTION

Up to the present, various models[1–11] have been advanced to describe the effect of uniaxial stress on magnetic properties. However, there has been very little theory developed for the case of uniaxial stress applied noncoaxially with the field.[12,13] Clearly, one major difference in this latter case is that many of the magnetic properties should have a dependence on the angle θ between field and stress axis.

In this article, we extend the magnetomechanical hysteresis model developed by Sablik and Jiles[7–9,11] to the case of noncoaxial stress and field. The model will be developed in several stages:

(1) Tensor relationships will be used to develop an angular dependence in the expression for the stress contribution H_σ to the effective field H_e.

(2) Since magnetostriction λ contributes to H_σ via its derivative $\partial\lambda/\partial M$, an angular dependence is also derived for the magnetostriction.

(3) Noncollinearity of magnetization M with the applied field H is considered and the resultant magnetization is obtained from contributions due to domain wall translation and domain wall bowing, in a manner similar to the magnetomechanical hysteresis model for coaxial stress and field.[7–9,11]

(4) The effect of roll-axis anisotropy is also included.

Numerical results from the model will be compared to experimental results for the case of stress axis perpendicular and parallel to the field.[14,15] Also, the predictions will be compared to experimental results obtained by Kaminski *et al.*[13,16] for stress axis and field at various angles.

II. FORMULATION OF THE STRESS CONTRIBUTION TO THE EFFECTIVE FIELD

The magnetomechanical hysteresis model for coaxial stress and field has been developed over a period of years.[7–9,11] A complete discussion of the model may be found in Ref. 17. The model is a macromagnetic model, distinguishing bulk magnetization and bulk magnetostriction, but not distinguishing domain wall types, as in the model of Schneider *et al.*[4,6,10]

In the magnetomechanical hysteresis model, the first step is to obtain an expression for the effective field, which includes an expression for the stress contribution H_σ to the effective field. The effective field H_e is determined from

$$H_e=\frac{1}{\mu_0}\left(\frac{\partial A}{\partial M}\right)_T, \tag{1}$$

where μ_0 is permeability of free space and A is the Helmholtz free energy density.[7] Since

$$A=G+\mu_0 HM\cos\beta, \tag{2}$$

$$G=U-TS+E_{me}^{\sigma}, \tag{3}$$

$$U=\tfrac{1}{2}\alpha\mu_0 M^2, \tag{4}$$

it follows that

$$H_e=H\cos\beta+\alpha M+\frac{1}{\mu_0}\frac{\partial E_{me}^{\sigma}}{\partial M}, \tag{5}$$

where G is the Gibbs free energy density, U is the internal energy density, α is the interdomain coupling constant, and β is the angle between the magnetization and field direction. E_{me}^{σ} is the magnetoelastic coupling energy density, given by

 0021-8979/93/74(1)/480/9/$6.00

$$E_{me}^{\sigma}=\sigma_{zz}e_{z'z'}^{me}, \tag{6}$$

where σ_{zz} is the applied uniaxial stress σ, taken to be along the z-axis, and where $e_{z'z'}^{me}$ is the magnetostrain developed along the direction of magnetization (here along the z' axis). The magnetostrain $e_{z'z'}^{me}$ may be expressed in x-y-z coordinates as[18]

$$e_{z'z'}^{me}=e_{zz}^{me}\cos^2\varphi+e_{yy}^{me}\sin^2\varphi-e_{yz}^{me}\sin\varphi\cos\varphi, \tag{7}$$

where ϕ is the angle between the magnetization and the stress axis. In an isotropic polycrystalline material, $e_{yz}=0$ and $e_{yy}=-\nu e_{zz}$, where ν is Poisson's ratio.[9,11,17] It therefore follows that

$$E_{me}^{\sigma}=\sigma[e_{zz}^{me}(\cos^2\varphi-\nu\sin^2\varphi)]. \tag{8}$$

This relationship has also been deduced by Kwun[12] from Barkhausen noise amplitudes for noncoaxial stress and field. Magnetostriction λ in this case is defined as the change in magnetostrain in the stress direction, and therefore[17,19]

$$\lambda=\tfrac{2}{3}[e_{zz}^{me}-(e_{zz}^{me})_0], \tag{9}$$

where $(e_{zz}^{me})_0$ is the magnetostrain in the demagnetized state. Note that magnetostrain is zero in the saturated state,[20] but that magnetostriction is zero in the demagnetized state.[17] It follows that the stress contribution to H_e is

$$H_\sigma=\frac{1}{\mu_0}\frac{\partial E_{me}^{\sigma}}{\partial M}$$
$$=\frac{\sigma}{\mu_0}\left[\frac{\partial}{\partial M}\left(\frac{3}{2}\lambda+(e_{zz}^{me})_0\right)\right](\cos^2\varphi-\nu\sin^2\varphi),$$

or

$$H_\sigma=\frac{3}{2}\frac{\sigma}{\mu_0}\frac{\partial\lambda}{\partial M}(\cos^2\varphi-\nu\sin^2\varphi). \tag{10}$$

Equation (10) was given previously without derivation.[13]

III. ANGULAR DEPENDENCE OF THE MAGNETOSTRICTION IN THE NONCOAXIAL STRESS AND FIELD CASE

The expression for H_σ depends on $d\lambda/dM$, but there is also an implicit angular dependence in $\lambda=\lambda(\phi)$.

We here follow our previous development for the magnetostriction,[9,11,17] but now incorporating angular dependence. The magnetostriction was derived via minimization of the energy density $E_{el}+E_{me}+\Phi_{\rm mag}$ with respect to the strains, which is necessary for mechanical equilibrium. These terms are

$$E_{el}=\tfrac{1}{2}C_{11}(e_{xx}^2+e_{yy}^2+e_{zz}^2)+\tfrac{1}{2}C_{44}(e_{xy}^2+e_{yz}^2+e_{zx}^2)$$
$$+C_{12}(e_{yy}e_{zz}+e_{xx}e_{yy}+e_{xx}e_{zz})-\sigma e_{zz}, \tag{11a}$$

$$E_{me}=B_1[e_{xx}(\alpha_1^2-\tfrac{1}{3})+e_{yy}(\alpha_2^2-\tfrac{1}{3})+e_{zz}(\alpha_3^2-\tfrac{1}{3})]$$
$$+B_2[e_{xy}\alpha_1\alpha_2+e_{yz}\alpha_2\alpha_3+e_{zx}\alpha_3\alpha_1], \tag{11b}$$

$$\Phi_{\rm mag}=\tfrac{1}{2}\alpha\mu_0M^2+\Phi_{\rm hys}, \tag{11c}$$

where

$$\alpha_1=0,\quad \alpha_2=\sin\phi,\quad \alpha_3=\cos\phi, \tag{12}$$

and where $\Phi_{\rm hys}$ is the extra magnetic energy density associated with magnetic hysteresis, which produces a departure of the system from the magnetization that it would have in thermodynamic equilibrium. Because the polycrystalline system is essentially isotropic on the macroscopic scale, it follows that

$$e_{xx}=e_{yy}=-\nu e_{zz}, \tag{13a}$$

$$e_{xy}=e_{yz}=e_{zx}=0, \tag{13b}$$

and the magnetoelastic coupling constants B_1 and B_2 may be written as

$$B_1=B_2=b. \tag{13c}$$

Isotropic (polycrystalline) conditions also imply that Poisson's ratio ν is given by

$$\nu=\frac{C_{12}}{(C_{11}+C_{12})} \tag{14a}$$

and that

$$C_{44}=\frac{(C_{11}-C_{12})}{2}. \tag{14b}$$

The condition for mechanical equilibrium then yields $\partial\Phi/\partial e_{xy}=\partial\Phi/\partial e_{yz}=\partial\Phi/\partial e_{zx}=0$, and

$$\frac{\partial\phi_{\rm mag}}{\partial e_{xx}}=\frac{1}{3}b, \tag{15a}$$

$$\frac{\partial\phi_{\rm mag}}{\partial e_{yy}}=\frac{1}{3}b(1-3\sin^2\phi), \tag{15b}$$

$$\frac{\partial\phi_{\rm mag}}{\partial e_{zz}}=\sigma+\frac{1}{3}b(1-3\cos^2\varphi)-Ye_{zz}, \tag{15c}$$

where Y is the Young's modulus given by[5,9]

$$Y=C_{11}-2C_{12}\nu. \tag{16}$$

Simplifying after integration and combining into a single equation yields

$$\frac{1}{2}Ye_{zz}^2+\left[-\sigma+\frac{2}{3}b(1+\nu)\left(1-\frac{3}{2}\sin^2\varphi\right)\right]e_{zz}$$
$$+\Phi_{\rm mag}+C=0. \tag{17}$$

Using the definition

$$b_\varphi\equiv b(1+\nu)(1-\tfrac{3}{2}\sin^2\varphi) \tag{18}$$

and the quadratic formula, one obtains

$$e_{zz}=\frac{\sigma}{Y}-\frac{2}{3}\frac{b_\varphi}{Y}\pm\sqrt{\frac{(\sigma-2/3b_\varphi)^2}{Y^2}-\frac{2(\Phi_{\rm mag}+C)}{Y}}. \tag{19}$$

The first term is the elastic contribution $e_{\rm el}=\sigma/Y$ and the rest is the magnetostrain e_{zz}^{me}. To find the integration constant C, one utilizes the condition that e_{zz}^{me} is zero at saturation.[20] After solving for C, one obtains

$$e_{zz}^{me}=-\frac{2}{3}\frac{b_\varphi}{Y}+\frac{b}{|b|}\sqrt{\left(\frac{2}{3}\frac{b_\varphi}{Y}\right)^2+\frac{2}{Y}[\Phi_{\rm mag}(M_s)-\Phi_{\rm mag}(M)]},\tag{20}$$

where M_s is the saturation magnetization. The plus sign is chosen in Eq. (20) so as to make e_{zz}^{me} equal to zero at saturation.

Now substituting this result for e_{zz}^{me} into Eq. (9), one obtains the following expression for the magnetostriction, namely that

$$\frac{3}{2}\lambda=\frac{b}{|b|}\left(\sqrt{\left(\frac{2}{3}\frac{b_\varphi}{Y}\right)^2+\frac{2}{Y}[\Phi_{\rm mag}(M_s)-\Phi_{\rm mag}(M)]^2}-\sqrt{\left(\frac{2}{3}\frac{b_\varphi}{Y}\right)^2+\frac{2}{Y}[\Phi_{\rm mag}(M_s)]^2}\right).\tag{21}$$

We see that λ depends on ϕ through its dependence on b_ϕ.

Note that in the expression for effective field stress contribution H_σ, one uses the thermodynamic result for $d\lambda/dM$, which does not include hysteresis. Thus, in substituting Eq. (21) into Eq. (10), one writes $\Phi_{\rm hys}=0$ and uses

$$\Phi_{\rm mag}(M)=\tfrac{1}{2}\mu_0\alpha M^2.\tag{22}$$

Also it has been shown[17] that the domain coupling constant α may be related to the saturation magnetostriction as

$$\alpha=[9Y\lambda_s^2/4\mu_0M_s^2][(\gamma+2)/\gamma)],\tag{23}$$

where

$$\gamma=[Y/(C_{11}-C_{12})]\{3/[2(1+\nu)]\}.\tag{23a}$$

IV. FORMULATION OF ANGULAR DEPENDENCE IN THE MAGNETIZATION

We here follow the development of the original magnetomechanical hysteresis formulation,[7–9,11] but with angular terms incorporated.

Thus, the total magnetization is given by the expression

$$M=M_{\rm rev}+M_i=c(M_a-M_i)+M_i,\tag{24}$$

where $M_{\rm rev}$ is the domain wall bending contribution[8,21] which involves reversible changes, and where M_i is the irreversible contribution to the magnetization due to domain wall translation. M_a is the anhysteretic magnetization (i.e., the magnetization in thermodynamic equilibrium, attained experimentally by imposing an ac component to the dc field H and gradually reducing the ac component to zero amplitude). The constant c is the ratio of the initial susceptibility $(\partial M/\partial H)$ at $H=0$ to the anhysteretic susceptibility $(dM_a/\partial H)$ at $H=0$.[21]

The irreversible contribution M_i can be obtained from the solution of

$$\frac{dM_i}{dH}=\frac{(M_a-M_i)\cos\beta}{\frac{\delta k}{\mu_0}-\left(\alpha+\frac{3}{2}\frac{\sigma}{\mu_0}\frac{d^2\lambda}{dM^2}(\cos^2\phi-\nu\sin^2\phi)\right)(M_a-M_i)}.\tag{25}$$

The derivation of this equation is similar to the one for dM_i/dH in case of coaxial stress and field.[7,17,21] The constant k is proportional to the pinning site density and the constant δ is ±1, depending on whether the applied field is increasing or decreasing.

The anhysteretic magnetization in the isotropic limit is given by[7,17,21]

$$M_a=M_s\mathscr{L}(H_e/a),\tag{26}$$

where $\mathscr{L}(x)=\cos x-1/x$ is the Langevin function, and where a is a constant that is proportional to the domain density in the demagnetized state.[17,21]

The angle β can be written as $\theta-\phi$, where θ is the angle between the stress axis and the field and where as stated earlier, ϕ is the angle between the magnetization and the stress axis. The angle θ is determined by the external conditions, but ϕ depends on internal constraints.

To obtain the angle ϕ, we minimize, with respect to ϕ, the thermodynamic work potential per unit volume, given as

$$\Omega=U-\mu_0HM\cos(\theta-\phi)-\tfrac{3}{2}\lambda\sigma(\cos^2\phi-\nu\sin^2\phi).\tag{27}$$

Note that in the case when the sign of the product $\lambda\sigma$ is positive the last term on the right-hand side reduces Ω when ϕ decreases. The second term reduces Ω when $\theta-\phi$ decreases. Physically, this says that for positive magnetostriction, tensile stress pulls the magnetization toward the stress axis, whereas compressive stress deflects the magnetization away from the stress axis. The magnetic field on the other hand always pulls the magnetization toward the field axis.

To a first approximation, we neglect here the dependence of λ on ϕ. The internal energy density U was given in Eq. (4). The equilibrium condition $d\Omega/d\phi=0$ results in

$$\cos\phi(\sin\phi+\eta\sin\theta)=\eta\cos\theta\sin\phi,\tag{28}$$

where

$$\eta=-\tfrac{1}{2}\mu_0HM/[\tfrac{3}{2}\lambda\sigma(1+\nu)].\tag{29}$$

By squaring Eq. (28) and substituting $\cos^2\phi=1-\sin^2\phi$, one obtains a quartic equation, namely

$$0=\sin^4\phi+2\eta\sin\theta\sin^3\phi+(\eta^2-1)\sin^2\phi-2\eta\sin\theta\sin\phi-\eta^2\sin^2\theta.\tag{30}$$

This quartic equation is solved numerically by Ferrari's method.[22]

V. INCLUSION OF ROLL-AXIS ANISOTROPY

Magnetic anisotropy, particularly that due to anisotropy introduced by the rolling of steel alloys, is discussed by Chikazumi and Charap.[23] For the purpose of this dis-

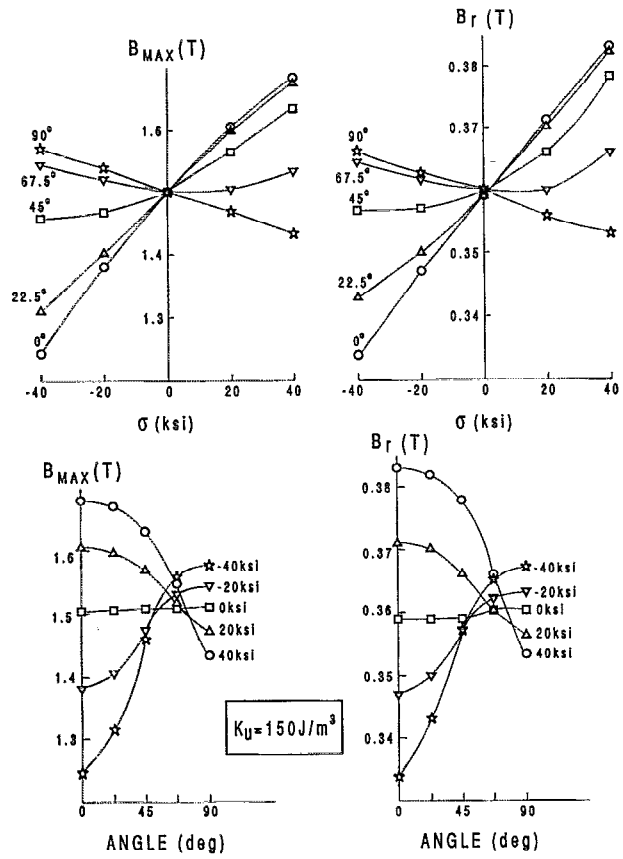

FIG. 1. Computed results for (a) maximum flux density (in tesla) and (b) remanence (in tesla) as a function of stress (in ksi) for five different angular orientations between magnetic field and stress axis. Also displayed are (c) maximum flux density and (d) remanence as a function of angle for five different stress values. For these cases, negligible roll axis anisotropy (K_u=150 J/m^3) is assumed.

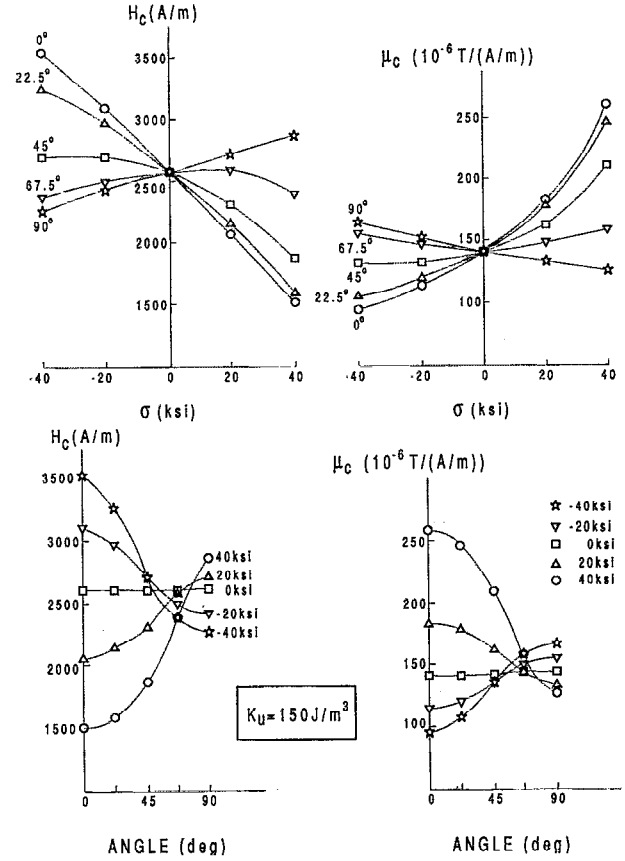

FIG. 2. Computed results in the case of negligible anisotropy for (a) coercivity H_c (in A/m) and (b) permeability μ_c at the coercive point [in 10^{-6} T/(A/m)] as a function of stress for five different angular orientations of stress and field. Also displayed are (c) H_c and (d) μ_c as a function of angle for five different stress values.

cussion, we shall consider only roll-axis anisotropy introduced in the same directon as that of the stress axis.

One can represent the energy density contribution due to such anisotropy as a uniaxial anisotropy of the form

$$E_u=-K_u\frac{M^2}{M_s^2}\cos^2\phi, \tag{31}$$

where a typical[23] numerical value for K_u is 7000 J/m^3.

The effective field with roll axis anisotropy included is then given by

$$H_e=H+\alpha_\phi M+\frac{3}{2}\frac{\sigma}{\mu_0}\frac{\partial\lambda}{\partial M}(\cos^2\phi-\nu\sin^2\phi), \tag{32}$$

where the domain coupling constant α is now altered by the roll-axis anisotropy, yielding an effective α_ϕ given by

$$\alpha_\phi=\alpha-\frac{2K_u}{\mu_0 M_s^2}\cos^2\phi. \tag{33}$$

The equation for the magnetization under these conditions is derived by a procedure similar to that in Eqs. (24)–(30), but with α in Eq. (25) replaced by α_ϕ. In obtaining a solution for ϕ, an additional term, namely $-K_u(M^2/M_s^2)\cos^2\phi$, is added to the right-hand side of Eq. (27) and η becomes

$$\eta=-\tfrac{1}{2}\mu_0 HM/[K_u M^2/M_s^2+3\lambda\sigma(1+\nu)/2]. \tag{34}$$

Otherwise, the derivation proceeds as before.

VI. NUMERICAL RESULTS

Figures 1–3 display the results of a numerical calculation for the case of K_u=150 J/m^3. The behavior for this case is essentially equivalent to the case of K_u=0. Thus, under zero stress, hysteresis loop parameters like maximum flux density (B_{max}), remanence (B_r), coercivity (H_c), and permeability at the coercive point (μ_c) all have the same value regardless of how the field is oriented relative to the axis chosen to be the stress axis. Under a nonzero stress, it makes a difference how the field is oriented relative to the stress axis.

The numerical curves in Figs. 1–3 are evaluated for $M_s=1.61\times10^6$ A/m, c=0.1, k/μ_0=3000 A/m, a=4500 A/m, $\lambda_s=20.7\times10^{-6}$, C_{11}=126 GJ/m^3, C_{12}=48 GJ/m^3, $b=-0.242\times10^{-2}$ GJ/m^3, and ν=0.276. For this combi-

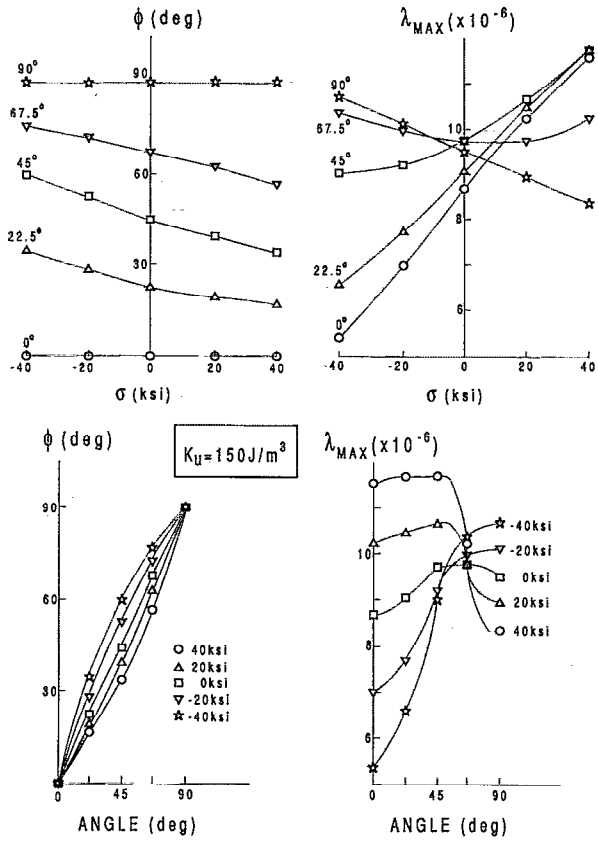

FIG. 3. Computed results in the case of negligible anisotropy for (a) angle ϕ between magnetization and stress axis and (b) maximum magnetostriction value λ_{max} as a function of stress for five different angles θ and as a function of angle θ for five different stress values. Note that there is no difference between θ and ϕ for $\theta=0°$ and for $\theta=90°$.

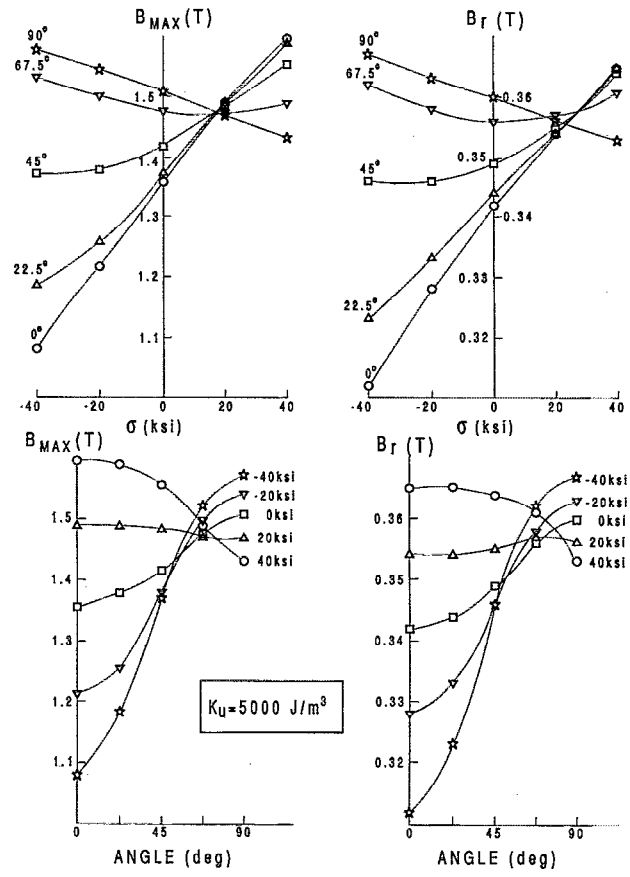

FIG. 4. Computed results when there is significant roll axis anisotropy ($K_u=5000$ J/m^3). Plotted are (a) maximum flux density B_{max} and (b) remanence B_r as a function of applied stress for five different angular orientations θ. Also displayed are (c) B_{max} and (d) B_r as a function of θ for five different values of applied stress.

nation, $\alpha=6.87\times10^{-5}$, as obtained from Eq. (23). In Figs. 1–3, stress σ is plotted in ksi (1 ksi=6.9 MPa).

Figure 1(a) shows plots B_{max} (in tesla) at $H=20$ kA/m vs stress σ (in ksi) for angles between field and stress axis given by 0°, 22.5°, 45°, 67.5°, and 90°. One notes that at zero angle, B_{max} is predicted to increase monotonically with stress, starting at negative stress (compression) and changing over to positive stress (tension). When field and stress axis are at 90°, the prediction is reversed, with B_{max} decreasing with stress, going from compression to tension. Nonmonotonic behavior is predicted for $\theta=67.5°$, with B_{max} decreasing with stress under compression and B_{max} first decreasing and then increasing under tension. The angles of 22.5° and 45° correspond to prediction of monotonically increasing behavior of B_{max} with stress.

The reason for the nonmonotonic behavior at $\theta=67.5°$ can be understood from Fig. 3(a), which shows a model calculation for angle ϕ as a function of stress. The change to what one might call "low angle" behavior, where B_{max} increases with stress, occurs at 20 ksi. From Fig. 3(a), ϕ is approximately 58° at 20 ksi and approximately 64° at zero ksi. The factor $\cos^2\phi-\nu\sin^2\phi$ appearing in H_σ changes from positive to negative as ϕ increases, equalling zero when $\phi=\tan^{-1}(\sqrt{1/\nu})=62.5°$. This is the angle ϕ_0 for which the change in behavior occurs in the stress dependence of B_{max}.

Figure 1(b) shows a model calculation for remanence B_r vs stress σ. The remanence is predicted to show behavior similar to that of B_{max} vs σ. Thus, B_r increases with increasing stress at zero angle and decreases with increasing stress at 90°. Again, the curve for $\theta=67.5°$ exhibits nonmonotonic behavior.

Figures 1(c) and 1(d) shows model predictions of families of curves for B_{max} vs θ and B_r vs θ, each curve corresponding to a different value of applied stress. For the high positive stresses, B_{max} and B_r are predicted to show decreases with increasing angle; whereas for high negative stresses, they exhibit increases with increasing angle. The curves tend to cross at $\theta=67.5°$, which is in the vicinity of the angle for $H_\sigma=0$, namely $\phi=\tan^{-1}(\sqrt{1/\nu})=62.5°$.

Figure 2(a) shows the behavior predicted by the model for coercivity H_c (in A/m) vs stress σ (in ksi). At zero angle, the coercivity is predicted to decrease with increasing stress, whereas at 90°, the opposite behavior occurs, with coercivity increasing with increasing stress. At 67.5°, the coercivity first increases, then decreases with in-

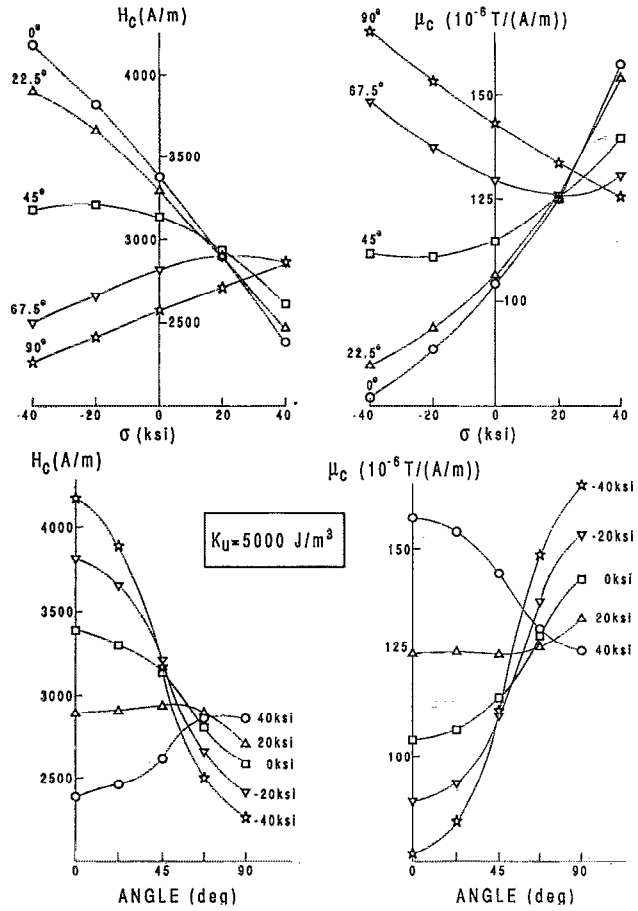

FIG. 5. Computed results in the case of $K_u=5000$ J/m^3 for (a) coercivity H_c and (b) permeability μ_c at the coercive point as a function of stress for five different θ. Also displayed are (c) H_c and (d) μ_c as a function of θ for five different values of stress.

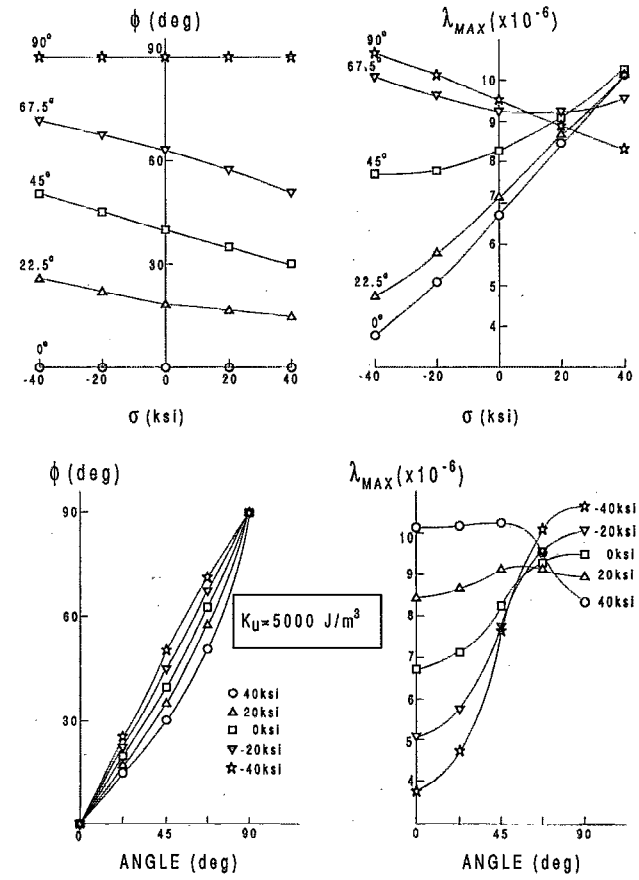

FIG. 6. Computed results in the case of $K_u=5000$ J/m^3 for (a) angle ϕ between magnetization and stress axis and (b) maximum magnetostriction value λ_{max} as a function of stress for five different angular orientations θ. Also displayed are (c) ϕ and (d) λ_{max} as a function of θ for five different stress values.

creasing stress, consistent with other nonmonotonic behavior predicted for $\theta=67.5°$.

The model prediction for the permeability μ_c at the coercive point is plotted against stress in Fig. 2(b). Here it is predicted that μ_c increases with increasing stress at zero angle and decreases with increasing stress at $\theta=90°$, in a manner similar to B_{max} and B_r. Again, at $\theta=67.5°$, nonmonotonic behavior is predicted.

Figures 2(c) and 2(d) display the predicted behavior for H_c vs θ and μ_c vs θ. At high positive stresses, H_c increases with increasing θ, whereas the opposite behavior is seen at high negative stresses. On the other hand, at high positive stresses, μ_c decreases with increasing θ, and at high negative stresses, increases with increasing θ. Again, $\theta=67.5°$ is an angle for which H_c and μ_c at the different stress levels remain approximately constant, representing the changeover from positive to negative H_σ in Eq. (10).

Figure 3(a) has been discussed earlier. However, we note here that at $\theta=0°$, one finds $\phi=0°$, as one might expect. Also at $\theta=90°$, so also is $\phi=90°$. In other words, ϕ only differs from θ when $0°<\theta<90°$. Note too that ϕ is larger under compression and smaller under tension. This is not surprising since tension should pull the magnetic moments toward the stress axis and compression should tend to push the moments away from the stress axis, for positive values of $d\lambda/dM$.

Figure 3(b) shows the variation of angle ϕ with angle θ at various stress levels. The figure displays the changes in ϕ at the various stress levels for different θ and shows $\phi=\theta$ at $\theta=0°$ or $\theta=90°$.

Figures 4–6 show the same set of curves as in Figs. 1–3 but with $K_u=5000$ J/m^3, so that roll-axis anisotropy is introduced. The main changes are that the plots against stress no longer cross at zero stress, but instead the crossing of stress values occurs at approximately 20 ksi or slightly higher. This is not surprising since when $\sigma=0$ and hence $H_\sigma=0$, there is still an angular effect which enters from the roll-axis anisotropy contribution to the effective field. At positive stress values, the H_σ contribution and the roll-axis contribution tend to cancel. Similarly, in the plot against angle θ, it is the 20 ksi curve and *not* the 0 ksi curve, which tends to show very little variation with angle.

VII. COMPARISON WITH EXPERIMENTAL RESULTS

Langman[15] has published data showing the variation of magnetic properties with uniaxial stress for angles of

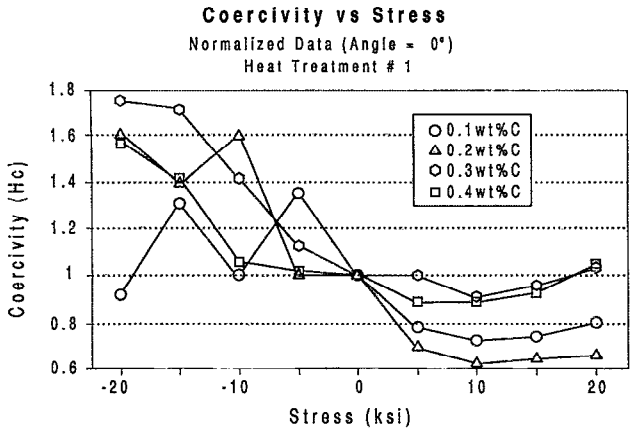

FIG. 7. Normalized experimental data for coercivity $[H_c/H_c(0)]$ against stress σ (in ksi). The stress ranges from -20 to $+20$ ksi. The coercivity values for $\sigma \neq 0$ are divided by the corresponding coercivity value at $\sigma=0$. Thus, for each material, the normalized value of coercivity at $\sigma=0$ is 1. In this plot, values are shown for spheroidized specimens containing 0.1, 0.2, 0.3, and 0.4 wt % C. In this case, the field and stress axis are coaxial ($\theta=0°$).

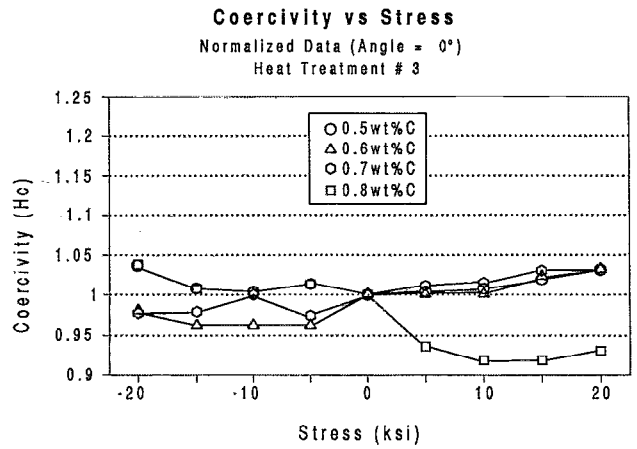

FIG. 9. Normalized experimental data for coercivity against stress (-20–$+20$ ksi). This time the specimens have been quenched and tempered and this time the compositions are 0.5, 0.6, 0.7, and 0.8 wt % C. In this case, the field and stress axis are coaxial ($\theta=0°$).

$\theta=0°$ and $\theta=90°$, i.e., for field parallel to the stress axis ($H_\parallel$ case) and for field perpendicular to the stress axis ($H_\perp$ case). In Fig. 2 of his article are displayed plots of B_{max} vs stress for various levels of maximum H.

The pattern seen by Langman is similar to that seen in Fig. 1(a). Under compression, $B_\parallel$ increases with increasing stress (i.e., decreasing compression) and $B_\perp$ decreases (but much more gradually) with increasing stress. Langman actually shows a slight increase, then a decrease in the behavior of $B_\perp$ under decreasing compression. This is due to what is commonly called the Villari effect and is a result of variations in the magnetoelastic coupling constant with stress (or equivalently, variations in λ_s with stress). In Ref. 7, we demonstrated how the Villari effect could be produced by assuming an *ad hoc* stress variation in λ_s.

Similarly, under tension, $B_\parallel$ continues at first to increase with increasing stress, but the variation is more gradual, with $B_\parallel$ exhibiting a peak and then small decrease with stress. Again, this is a result of the Villari effect. Under tension, $B_\perp$ decreases with increasing stress, similar to the behavior predicted in Fig. 1(a).

The trends seen by Langman thus are predicted by our model, except for the Villari effect, which can be added to the model by providing a stress dependence for the magnetoelastic coupling constant b.

Figures 7 and 8 show experimental data taken at Ames Laboratory of the variation of coercivity with stress from -20 to 20 ksi for the cases of $\theta=0°$ and $\theta=90°$, respectively. The data is normalized by the value of coercivity at zero stress. The four different plots are for carbon steels with different percentages of carbon, namely 0.1, 0.2, 0.3, and 0.4 wt % C. The steel was heat treated after being cast.

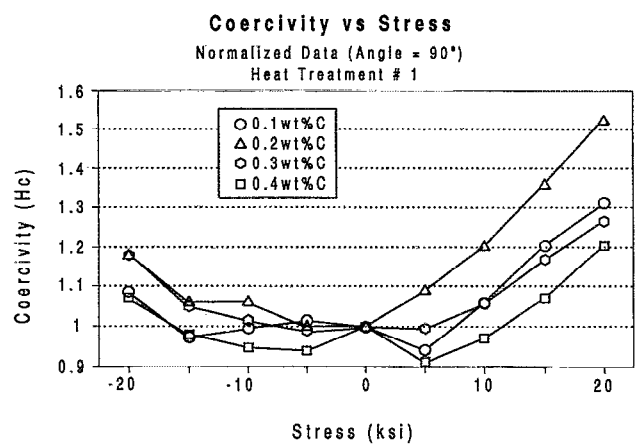

FIG. 8. Normalized experimental data for coercivity against stress (again from -20 ksi to $+20$ ksi and again for 0.1, 0.2, 0.3, and 0.4 wt % C). This time, however, the field and stress axis are perpendicular ($\theta=90°$).

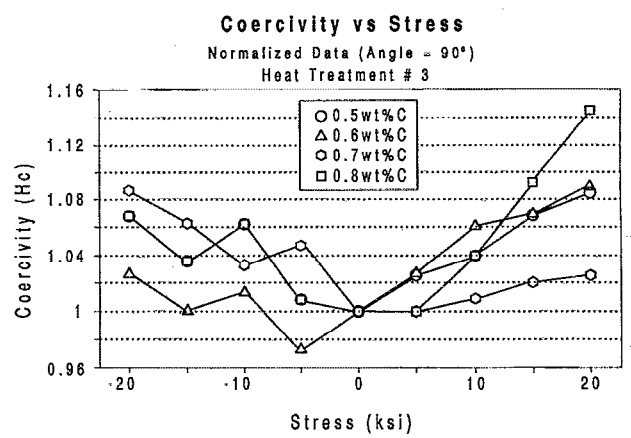

FIG. 10. Normalized experimental data for coercivity against stress (-20–$+20$ ksi). Again, the plots are for 0.5, 0.6, 0.7, and 0.8 wt % C. This time the field and stress axis are perpendicular ($\theta=90°$).

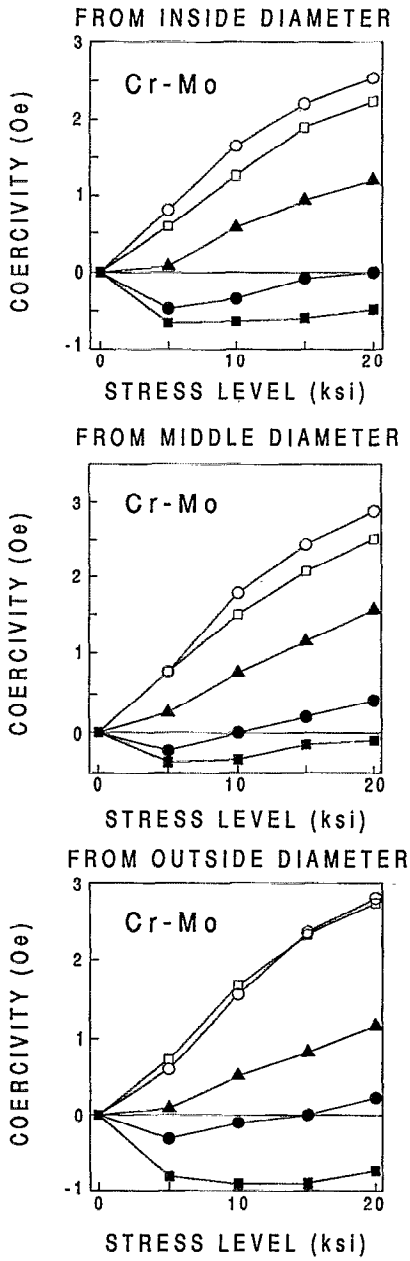

FIG. 11. Coercivity difference $H_c(\sigma)-H_c(0)$ vs stress data for 2.25% Cr and 1.0% Mo chrome-molybdenum steel that was cut from a steam pipe that had been in service in a power plant. The five different plots on each figure are for five different angular orientations, as follows: ■ 0°, ● 18.4°, ▲ 45°, □ 71.6°, ○ 90°. As labeled, the different figures are from specimens taken from (a) the inside diameter, (b) the middle diameter, and (c) the outside diameter of the pipe.

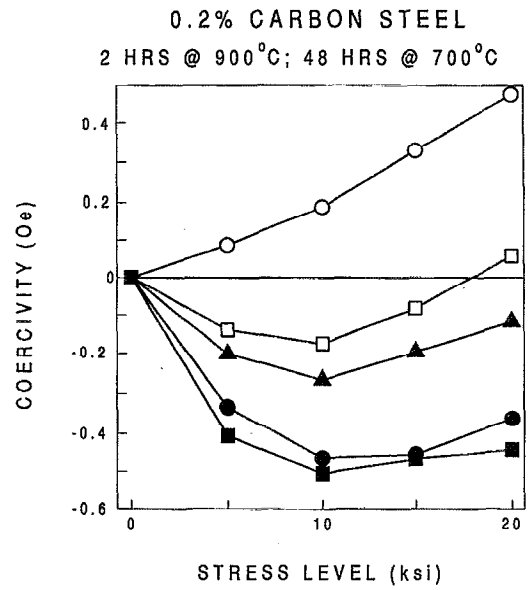

FIG. 12. Coercivity vs stress data for 0.2% carbon steel for five different angular orientations, as labeled. Difference $H_c(\sigma)-H_c(0)$ is plotted, just as in Fig. 11. Symbols for the different angles,are the same as in Fig. 11.

In this spheroidization heat treatment, the steel was held at 900 °C for 2 h then held at 700 °C for 48 h. Clearly in Fig. 7, with the applied field at $\theta=0°$ relative to the stress axis, the trend is a reduction in coercivity as the stress changes from -20 to $+20$ ksi. This is the trend seen in Fig. 2(a) for $\theta=0°$. The experimental variation differs from the predicted variations at positive stresses, in that the experimental tendency is for the coercivity to reach a minimum, then increase slightly. This is again due to the Villari effect. The experimental variation seen in Fig. 8 for $\theta=90°$ is essentially the opposite of that seen in Fig. 7. The trend is an increase in coercivity as stress increases from -20 to 20 ksi. This time at $\theta=90°$ the coercivity minimum occurs for negative stresses.

Similar but slightly less distinct behavior is seen for the coercivity in Figs. 9 and 10. These figures are for steel heat treated in a different manner. In this quenched heat treatment, the steel was held at 950 °C for 2 h, then water quenched, then annealed at 700 °C for 2 h. In this case, the carbon percentages are 0.5, 0.6, 0.7, and 0.8 wt % C. Here there is a much smaller variation of coercivity with stress. In Fig. 9, at $\theta=0°$, there is at best a very slight overall reduction in coercivity with increasing stress, although possibly a better description would be to say that to within experimental error ($\pm 5\%$), there is essentially no change to be distinguished. In Fig. 10, at $\theta=90°$, the behavior is similar to that in Fig. 8, with a Villari minimum at negative stress and an increase in coercivity at positive stresses. In this case, the minimum is lost in the experimental error ($\pm 5\%$), and the trends described in Fig. 8 can only be barely distinguished in Fig. 10.

Figures 11(a)–11(c) show coercivity data for chromium-molybdenum steel containing 2.25 wt % Cr and 1 wt % Mo. This type of steel is used for steam pipes in power plants. In this case, the steel was cut from a pipe that previously had been in service in a power plant. Figures 11(a)–11(c) are for steel cut from (a) the inside diameter, (b) the middle diameter, and (c) the outside diameter of the pipe. The figures show the coercivity difference $H_c(\sigma)-H_c(0)$ (in Oe) against applied tensile stress for different angles between the magnetic field H and the stress axis. One should note that at $\theta=90°$, the coercivity increases with increasing stress, as predicted by Fig.

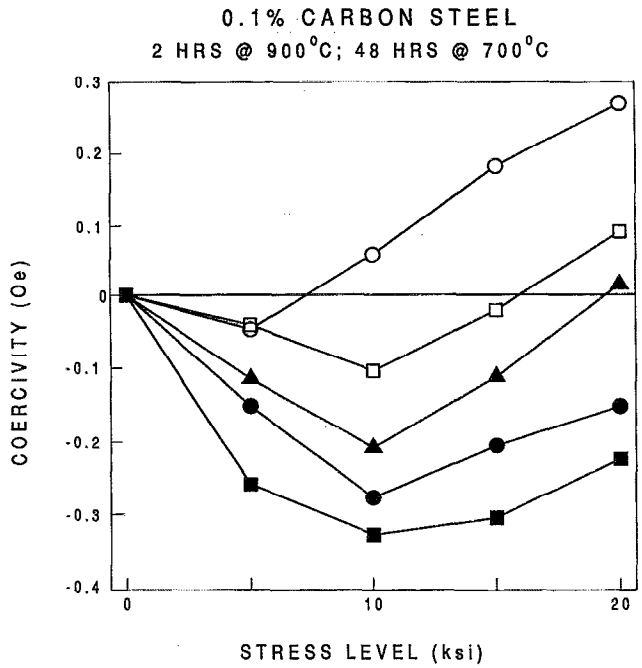

FIG. 13. Coercivity vs stress data for 0.1% carbon steel for five different angular orientations, as labeled. Again, difference $H_c(\sigma)-H_c(0)$ is plotted. Again, symbols for the different angular orientations are as in Fig. 11.

2(a) and as seen earlier in Figs. 8 and 10. Similarly at $\theta=0°$, the decrease to the Villari minimum is seen, again as in Figs. 7 and 9.

A similar coercivity plot is seen in Fig. 12, this time for spheroidized 0.2 wt % C carbon steel. In this case, the crossover from $\theta=0°$ behavior to $\theta=90°$ behavior occurs slightly differently for the in-between angles. Figure 13 displays the results for spheroidized 0.1 wt % C steel.

It should be mentioned here that all the experimental data displayed was taken at Ames Laboratory using a probe that could be brought up to the sample surface. Windings were not wrapped around the sample to determine flux density in the sample itself. Thus, the signal actually measured the flux density of the core in the probe. But, of course, the signal was duly influenced by the properties of the sample, which in turn couple to the stresses in the sample. Mathematical analysis should allow the intrinsic magnetic properties of the test material to be determined from such measurements. The reason why we have shown only coercivity plots is that the flux density measured in the probe's magnetic core should be proportional to the flux density in the sample. Thus, both flux densities are zero at the same time, and the measured hysteresis loop exhibits the same coercivity as found in the sample itself. We are presently exploring procedures for extracting the other magnetic properties of the test material from the measured hysteresis curves.

VIII. CONCLUSION

The general angular trends seen in the experimental data are predicted by the model, except that the Villari effect is not presently incorporated in the model.

Thus, at $\theta=0°$, coercivity tends to decrease in going from negative stress to positive stress, as predicted by the model, and as shown in Fig. 2. Experimentally, the Villari effect is seen at positive stresses, as seen in Figs. 7 and 11–13, in that the coercivity decreases to a minimum and then increases slightly. At 90°, the opposite behavior is seen experimentally with coercivity increasing from negative to positive stress as predicted by the model, as shown in Fig. 2. Experimentally, at negative stresses, the Villari minimum is seen, as shown in Figs. 8 and 10.

Similarly, at $\theta=0°$, the model predicts that maximum flux density increases from negative to positive applied stress, as shown in Fig. 1. A Villari maximum is additionally found for positive stress experimentally.[14,15] At $\theta=90°$, the model predicts that maximum flux density displays the opposite behavior, decreasing from negative to positive stress. Experimentally, a Villari maximum is found at negative stress.

In the future, we have plans for a method of incorporating the Villari effect into the model predictions via a stress dependence in $d\lambda/dM$. We also plan to investigate more closely the effect of microstructure and material properties on the magnetic response.

ACKNOWLEDGMENT

This work was supported by the Electric Power Research Institute Contract No. RP2426-29.

[1] R. Becker and M. Kersten, Z. Physik **64**, 660 (1930).
[2] W. F. Brown, Phys. Rev. **75**, 147 (1949).
[3] R. R. Birss, IEEE Trans. Magn. **1**, 113 (1971).
[4] C. S. Schneider and E. A. Semcken, J. Appl. Phys. **52**, 2425 (1981).
[5] M. L. Spano, K. B. Hathaway, and H. T. Savage, J. Appl. Phys. **53**, 2667 (1982).
[6] C. S. Schneider and M. Charlesworth, J. Appl. Phys. **57**, 4198 (1985).
[7] M. J. Sablik, H. Kwun, G. L. Burkhardt, and D. C. Jiles, J. Appl. Phys. **63**, 3930 (1988).
[8] M. J. Sablik, Nondestr. Test. Eval. **5**, 49 (1989).
[9] M. J. Sablik and H. Kwun, J. Appl. Phys. **69**, 5791 (1991).
[10] C. S. Schneider, P. Y. Cannell, and K. T. Watts, IEEE Trans. Magn. **28**, 2626 (1992).
[11] M. J. Sablik and S. W. Rubin, J. Magn. Magn. Mater. **104-107**, 392 (1992).
[12] H. Kwun, J. Magn. Magn. Mater. **49**, 235 (1985).
[13] D. A. Kaminski, D. C. Jiles, S. B. Biner, and M. J. Sablik, J. Magn. Magn. Mater. **104-107**, 382 (1992).
[14] R. Langman, NDT International **14**, 255 (1981).
[15] R. Langman, IEEE Trans. Magn. **21**, 1314 (1985).
[16] D. A. Kaminski, D. Jiles, S. B. Biner, and M. J. Sablik, Proceedings of the QNDE Conference, La Jolla, California, July 1992 (to be published).
[17] M. J. Sablik and D. C. Jiles, IEEE Trans. Magn. (to be published).
[18] A. E. H. Love, *A Treatise on the Mathematical Theory of Elasticity*, 4th ed. (Dover, New York, 1944), p. 107.
[19] S. Chikazumi and S. H. Charap, *Physics of Magnetism* (Krieger, Malabar, 1984), p. 163.
[20] B. D. Cullity, *Introduction to Magnetic Materials* (Addison–Wesley, Reading, MA, 1972), pp. 283–284.
[21] D. C. Jiles and D. L. Atherton, J. Magn. Magn. Mater. **61**, 48 (1986).
[22] N. B. Conkwright, *Introduction to the Theory of Equations* (Ginn and Company, Boston, MA, 1941), pp. 78–79.
[23] S. Chikazumi and S. H. Charap, *ibid.*, Chap. 17.